

SCU (AF

Classified and is  
R 150-12

**CAMBRIDGE HYDRODYNAMICS FINAL REPORT**  
**ADVANCED NUMERICAL METHODS FOR THREE-  
DIMENSIONAL PARALLEL HYBRID MHD/PIC**

**Contract # F49620-94-C-0034**

dissemination

by

**DTIC QUALITY INSPECTED 2**

Cambridge Hydrodynamics, Inc.  
P.O. Box 1403  
Princeton, NJ 08542

(609) 683-1515

<b>DISTRIBUTION STATEMENT A</b>
Approved for public release;
Distribution Unlimited

19970604 157

# REPORT DOCUMENTATION PAGE

Form Approved  
OMB No. 0704-0188

Public reporting burden for this collection of information is estimated to average 1 hour per response, including the time for reviewing instructions, searching existing data sources, gathering and maintaining the data needed, and completing and reviewing the collection of information. Send comments regarding this burden estimate or any other aspect of this collection of information, including suggestions for reducing this burden, to Washington Headquarters Services, Directorate for Information Operations and Reports, 1215 Jefferson Davis Highway, Suite 1204, Arlington, VA 22202-4302, and to the Office of Management and Budget, Paperwork Reduction Project (0704-0188), Washington, DC 20503.

1. AGENCY USE ONLY (Leave blank)		2. REPORT DATE Oct. 31, 1996	3. REPORT TYPE AND DATES COVERED Final May 1, 1994-Oct. 31, 1996	
4. TITLE AND SUBTITLE Advanced Numerical Methods for Three-Dimensional Parallel Hybrid MHD/PIC			5. FUNDING NUMBERS F49620-94-C-0034 AFOSR Contract	
6. AUTHOR(S) Robert L. McCrory, Steven A. Orszag, Alexandr Konstantinov, Ilya Staroselsky, Charles P. Verdon				
7. PERFORMING ORGANIZATION NAME(S) AND ADDRESS(ES) Cambridge Hydrodynamics, Inc. P.O. Box 1403 Princeton, NJ 08542			8. PERFORMING ORGANIZATION REPORT NUMBER	
9. SPONSORING/MONITORING AGENCY NAME(S) AND ADDRESS(ES) Air Force of Scientific Research 110 Duncan Avenue, Suite B115 Bolling AFB, DC 20332-0001			10. SPONSORING/MONITORING AGENCY REPORT NUMBER	
11. SUPPLEMENTARY NOTES				
12a. DISTRIBUTION/AVAILABILITY STATEMENT Unclassified/Unlimited			12b. DISTRIBUTION CODE	
13. ABSTRACT (Maximum 200 words)  We have developed, implemented, and applied coupled Eulerian/Lagrangian computational models for efficient parallel numerical simulation of high energy density plasmas. Prototype problems include studies of physical systems encountered in advanced weapons, space propulsion thrusters, pulsed power systems, and other areas of direct interest to the Air Force. The main conclusion of our study is that computationally efficient and physically sound description of nonsteady plasmas typical for these applications is possible using the advanced hybrid MHD/PIC methods developed here.  In the first chapter of this report, we outline technical details of our computational approach, including numerical algorithms, physical models, and efficient numerical implementation strategies evaluated/implemented during this work. In the second chapter, we discuss several representative flow simulations obtained using computational models developed as a result of our research. In particular, we have investigated optimal regimes of plasma focusing and energy conversion across a wide range of parameters and devices geometries. Overall, our results show that, with advanced parallel computing platforms, analysis and prototyping of certain plasma device components of interest to the Air Force are amenable to cost efficient numerical simulation.				
14. SUBJECT TERMS			15. NUMBER OF PAGES 50	
			16. PRICE CODE	
17. SECURITY CLASSIFICATION OF REPORT Unclassified	18. SECURITY CLASSIFICATION OF THIS PAGE Unclassified	19. SECURITY CLASSIFICATION OF ABSTRACT Unclassified	20. LIMITATION OF ABSTRACT	

## GENERAL INSTRUCTIONS FOR COMPLETING SF 298

The Report Documentation Page (RDP) is used in announcing and cataloging reports. It is important that this information be consistent with the rest of the report, particularly the cover and title page. Instructions for filling in each block of the form follow. It is important to *stay within the lines* to meet optical scanning requirements.

**Block 1. Agency Use Only (Leave blank).**

**Block 2. Report Date.** Full publication date including day, month, and year, if available (e.g. 1 Jan 88). Must cite at least the year.

**Block 3. Type of Report and Dates Covered.** State whether report is interim, final, etc. If applicable, enter inclusive report dates (e.g. 10 Jun 87 - 30 Jun 88).

**Block 4. Title and Subtitle.** A title is taken from the part of the report that provides the most meaningful and complete information. When a report is prepared in more than one volume, repeat the primary title, add volume number, and include subtitle for the specific volume. On classified documents enter the title classification in parentheses.

**Block 5. Funding Numbers.** To include contract and grant numbers; may include program element number(s), project number(s), task number(s), and work unit number(s). Use the following labels:

C - Contract	PR - Project
G - Grant	TA - Task
PE - Program Element	WU - Work Unit Accession No.

**Block 6. Author(s).** Name(s) of person(s) responsible for writing the report, performing the research, or credited with the content of the report. If editor or compiler, this should follow the name(s).

**Block 7. Performing Organization Name(s) and Address(es).** Self-explanatory.

**Block 8. Performing Organization Report Number.** Enter the unique alphanumeric report number(s) assigned by the organization performing the report.

**Block 9. Sponsoring/Monitoring Agency Name(s) and Address(es).** Self-explanatory.

**Block 10. Sponsoring/Monitoring Agency Report Number.** (If known)

**Block 11. Supplementary Notes.** Enter information not included elsewhere such as: Prepared in cooperation with...; Trans. of...; To be published in.... When a report is revised, include a statement whether the new report supersedes or supplements the older report.

**Block 12a. Distribution/Availability Statement.** Denotes public availability or limitations. Cite any availability to the public. Enter additional limitations or special markings in all capitals (e.g. NOFORN, REL, ITAR).

DOD - See DoDD 5230.24, "Distribution Statements on Technical Documents."

DOE - See authorities.

NASA - See Handbook NHB 2200.2.

NTIS - Leave blank.

**Block 12b. Distribution Code.**

DOD - Leave blank.

DOE - Enter DOE distribution categories from the Standard Distribution for Unclassified Scientific and Technical Reports.

NASA - Leave blank.

NTIS - Leave blank.

**Block 13. Abstract.** Include a brief (*Maximum 200 words*) factual summary of the most significant information contained in the report.

**Block 14. Subject Terms.** Keywords or phrases identifying major subjects in the report.

**Block 15. Number of Pages.** Enter the total number of pages.

**Block 16. Price Code.** Enter appropriate price code (*NTIS only*).

**Blocks 17. - 19. Security Classifications.** Self-explanatory. Enter U.S. Security Classification in accordance with U.S. Security Regulations (i.e., UNCLASSIFIED). If form contains classified information, stamp classification on the top and bottom of the page.

**Block 20. Limitation of Abstract.** This block must be completed to assign a limitation to the abstract. Enter either UL (unlimited) or SAR (same as report). An entry in this block is necessary if the abstract is to be limited. If blank, the abstract is assumed to be unlimited.

# Chapter 1

## Introduction

In this Report, we summarize results obtained with support of the Air Force Contract F49620-94-C-0034. As a result of this effort we have developed, implemented, and applied several Eulerian/Lagrangian computational models for efficient numerical simulation of high energy density plasmas. Prototype setups studied in this project are modeled after physical systems encountered in advanced weapons, space propulsion thrusters, pulsed power systems, and other areas of direct interest to the Air Force. The main conclusion of our study is that computationally efficient and physically sound description of nonsteady plasmas typical for these applications is possible using the advanced hybrid MHD/PIC methods developed here.

In Section 1, we outline technical details of our computational approach, including numerical algorithms, physical models, and efficient numerical implementation strategies evaluated/implemented during this work. In Section 2, we discuss several representative flow simulations obtained using computational models developed as a result of our research. In particular, we have investigated optimal regimes of plasma focusing and energy conversion across a range of plasma beam parameters. Overall, our results show the prospect that using advanced platforms developed in this project, analysis and prototyping of certain plasma device components of interest to the Air Force are amenable to cost efficient numerical simulation.

# Chapter 2

## Computational Model

Here we describe technical details of our numerical algorithms and implementation strategies used for physical modeling of high energy density plasmas of interest in this project. Two main codes will be described, RIGEL and ELPIC-MHD, which have been developed here.

### 2.1 Physical Models

#### 2.1.1 Gyrokinetic/MHD Hybrid Scheme and Applicability Limits

Fluid Equations

$$\rho \frac{\partial}{\partial t} \mathbf{v} + \rho (\mathbf{v} \cdot \nabla) \mathbf{v} = -\nabla p - (\nabla \cdot \mathbf{P}_h)_\perp + \mathbf{J} \times \mathbf{B} \quad (1)$$

$$\frac{\partial}{\partial t} \mathbf{B} = \nabla \times \mathbf{E}, \quad \mathbf{E} = (\mathbf{v} \times \mathbf{B} - \eta \mathbf{J}), \quad \mathbf{J} = \nabla \times \mathbf{B} \quad (2)$$

$$\frac{\partial}{\partial t} \rho + \nabla \cdot (\rho \mathbf{v}) = 0 \quad (3)$$

$$\frac{\partial}{\partial t} p + \mathbf{v} \cdot \nabla p = -\gamma p \nabla \mathbf{v} + \rho \nabla_{\parallel} \cdot \kappa_{\parallel} \nabla_{\parallel} (p/\rho) \quad (4)$$

$$\nabla_{\perp}^2 \mathbf{A} = -\mathbf{J}_{\perp} \quad (5)$$

Gyrokinetic equations for energetic particles

$$\mathbf{P}_h = P_{\perp} \mathbf{I} + (P - P_{\perp}) \mathbf{b} \mathbf{b}, \quad (6)$$

$$P_{\parallel} = \int d^3 v F(m u^2), \quad P_{\perp} = \int d^3 v F(\mu B) \quad (7)$$

$$F = F(\mathbf{R}, u, \mu)$$

$$d\mathbf{R}/dt = u[ \mathbf{b} + (u/\Omega) \mathbf{b} \times (\mathbf{b} \cdot \nabla) \mathbf{b} ] + (1/\Omega) \mathbf{b} \times (\mu \nabla B - q \mathbf{E}/m) \quad (8)$$

$$du/dt = - [ \mathbf{b} + (u/\Omega) \mathbf{b} \times (\mathbf{b} \cdot \nabla) \mathbf{b} ] \cdot (\mu \nabla B - q \mathbf{E}/m) \quad (9)$$

$$\left(\frac{\rho}{\lambda_D}\right)^2 \nabla_{\perp}^2 \phi = -e(n_i - n_e) \quad (10)$$

Efficient implementation of the fast Laplace solvers involved here represented an important part of this effort.

The plasma can be modeled as single-component fluid with transport coefficients independent of  $\mathbf{B}$  under the following conditions. Let us introduce the following notation:

$\omega$  is the typical flow frequency ( $\partial/\partial t$  is of the order of  $\omega$ ),

$\tau_e, \tau_i$  are the electron-electron and the ion-ion collision times, respectively,

$\Omega_i$  is the ion cyclotron frequency,

$v_T^e, v_T^i$  are the electron/ion thermal velocities, respectively,

$v_A$  is the Alfven velocity,

$\rho_B^i$  is the ion Larmor radius,

$\rho_D^i$  is the ion Debye radius,

$\lambda_e, \lambda_i$  are the mean free paths of the electrons and ions respectively,

$\Pi_e \equiv ne^2/(m_e \epsilon_0)$  is the electron plasma frequency.

The first condition necessary condition for the MHD approach to hold implies that the plasma is in a quasi-stationary state characterized by a frequency  $\omega$  which is much lower than the effective frequency of electron-ion collisions:

$$\frac{1}{\omega} \gg \tau_e, \tau_i \quad \frac{v_T^{e,i}}{\omega} \gg \lambda_{e,i} \quad (11)$$

In this case the particle distribution function can be considered to be isotropic. Another set of conditions

$$\omega \ll \Omega_i \quad \frac{v_T^i}{\omega} \gg \rho_B^i \quad (12)$$

$$L \gg \min(\lambda_i, \rho_B^i), \quad L \gg \rho_D^i \quad (13)$$

results in Ohm's law written as follows

$$\mathbf{j} = \sigma \left( \mathbf{E} + \mathbf{v} \times \mathbf{B} - \frac{1}{en_e} \nabla p_i \right), \quad (14)$$

where  $e$  is the electron charge,  $n_e$  is the electron number density, and  $p_i$  is the ion pressure. When  $|\nabla p_i/n| \approx |\nabla T_i| \ll |eE|$  ( $T_i$  being the ions temperature), the  $\nabla p_i$  term may be neglected. Then, Ohm's and Ampere's laws take the following form

$$\frac{\mathbf{j}}{\sigma} = \mathbf{E} + \mathbf{v} \times \mathbf{B} \quad (15)$$

$$\mu \mathbf{j} = \nabla \times \mathbf{B} \quad (16)$$

If the following condition holds

$$\frac{\Pi_e^2 \tau_e}{\omega} \gg 1, \quad (17)$$

then the displacement current may be omitted in the Maxwell equation which reduces to

$$\frac{\partial \mathbf{B}}{\partial t} = -\nabla \times \mathbf{E} \quad (18)$$

The standard MHD field equation is readily obtained from equations (15), (16) and (18).

Let us now look at specific figures. Some relevant plasma parameters in mks units are<sup>2,5</sup>:

$$\tau_e = \frac{25.8\pi^{1/2}\epsilon_0^2 m_e^{1/2} T_e^{3/2}}{n_e e^4 \ln \Lambda} = 3.3 \times 10^{-9} \frac{1}{\ln \Lambda} \left(\frac{T_e}{e}\right)^{3/2} \left(\frac{n_e}{10^{20}}\right)^{-1} \quad (19)$$

$$\tau_i = \frac{25.8\pi^{1/2}\epsilon_0^2 m_i^{1/2} T_i^{3/2}}{n_e Z^4 e^4 \ln \Lambda} = 1.4 \times 10^{-7} \frac{A^{1/2}}{Z^4} \frac{1}{\ln \Lambda} \left(\frac{T_i}{e}\right)^{3/2} \left(\frac{n_i}{10^{20}}\right)^{-1} \quad (20)$$

$$\Omega_i = \frac{ZeB}{m_i} = 9.58 \times 10^7 \frac{Z}{A} B \quad (21)$$

$$v_T^e = \left(\frac{T_e}{m_e}\right)^{1/2} = 4.19 \times 10^5 \left(\frac{T_e}{e}\right)^{1/2} \quad (22)$$

$$v_T^i = \left(\frac{T_i}{m_i}\right)^{1/2} = 9.79 \times 10^3 \left(\frac{T_i}{Ae}\right)^{1/2} \quad (23)$$

$$v_A = \left(\frac{B^2/\mu}{n_i m_i}\right)^{1/2} = 2.18 \times 10^6 B \left(\frac{An_i}{10^{20}}\right)^{-1/2} \quad (24)$$

$$\rho_B^i = \left(\frac{T_i}{m_i}\right)^{1/2} \frac{1}{\Omega_i} = 1.02 \times 10^{-4} \frac{1}{Z} \left(\frac{AT_i}{e}\right)^{1/2} \frac{1}{B} \quad (25)$$

$$\rho_D^e = \left(\frac{\epsilon_0 T_e}{n_e e^2}\right)^{1/2} = 7.45 \times 10^{-7} \left(\frac{T_e}{e}\right)^{1/2} \left(\frac{n_e}{10^{20}}\right)^{-1} \quad (26)$$

$$\lambda_e = \left(\frac{3T_e}{m_e}\right)^{1/2} \tau_e = 2.4 \times 10^{-3} \frac{1}{\ln \Lambda} \left(\frac{T_e}{e}\right)^2 \left(\frac{n_e}{10^{20}}\right)^{-1} \quad (27)$$

$$\lambda_i = \left(\frac{3T_i}{m_i}\right)^{1/2} \tau_i = 2.4 \times 10^{-3} \frac{1}{Z^4 \ln \Lambda} \left(\frac{T_i}{e}\right)^2 \left(\frac{n_i}{10^{20}}\right)^{-1} \quad (28)$$

$$\Pi_e = \left(\frac{n_e e^2}{m_e \epsilon_0}\right)^{1/2} = 5.64 \times 10^{11} \left(\frac{n_e}{10^{20}}\right)^{1/2} \quad (29)$$

Here  $Ze$  is the electrical charge of ions,  $A$  is the atomic weight of ions, and  $\ln \Lambda$  is the Coulomb logarithm,

$$\ln \Lambda \approx 7 + 2.3 \log_{10} \left( \left(\frac{T_e}{e}\right)^{3/2} / \left(\frac{n_e}{10^{20}}\right)^{1/2} \right) \quad (30)$$

For the plasma electron temperature  $T_e/e$  of 10 eV and the electron number density of  $10^{24} m^{-3}$  we obtain  $\ln \Lambda \approx 6$ ,  $\tau_e \approx 2 \times 10^{-12} s$ ,  $\tau_i \approx 10^{-9}/Z^4 s$ ,  $\Omega_i \approx 10^6 ZB s^{-1}$ ,  $\lambda_e \approx 4 \times 10^{-6} m$ ,  $\lambda_i \approx 4 \times 10^{-6}/Z^4 m$ ,  $v_T^e \approx 10^6 m/s$ ,  $v_T^i \approx 3 \times 10^3 m/s$ ,  $v_A \approx 2 \times 10^3 B m/s$ ,  $\rho_B^i \approx 3 \times 10^{-3}/(ZB) m$ ,  $\Pi_e \approx 6 \times 10^{13} s^{-1}$ . Substituting another typical set of values



of  $T_e/e = 100\text{eV}$  and  $n_e = 10^{25}$  yields  $\ln\Lambda \approx 8$ ,  $\tau_e \approx 4 \times 10^{-12}\text{s}$ ,  $\tau_i \approx 2 \times 10^{-9}/Z^4\text{s}$ ,  $\Omega_i \approx 10^6 ZB\text{s}^{-1}$ ,  $v_T^i \approx 10^4\text{m/s}$ ,  $\rho_B^i \approx 10^{-2}/(ZB)m$ ,  $\Pi_e \approx 2 \times 10^{14}\text{s}^{-1}$ . In both cases all the conditions (11) - (13) and (17) hold with confidence.

### 2.1.2 The MHD approximation

The Eulerian form of the MHD equations implemented in our numerical scheme is as follows:

Hydrodynamic equations

$$\frac{\partial \mathbf{v}}{\partial t} + (\mathbf{v} \cdot \nabla)\mathbf{v} = -\frac{1}{\rho}\nabla P + \nu\nabla^2\mathbf{v} + \frac{1}{3}\nu\nabla(\nabla \cdot \mathbf{v}) + \frac{1}{\rho}\mathbf{j} \times \mathbf{B} \quad (31)$$

$$\frac{\partial \rho}{\partial t} + \nabla \cdot (\rho\mathbf{v}) = 0 \quad (32)$$

Magnetohydrodynamic equations

$$\frac{\partial \mathbf{B}}{\partial t} = \frac{1}{\mu\sigma}\nabla^2\mathbf{B} + \nabla \times (\mathbf{v} \times \mathbf{B}) \quad (33)$$

$$\mu\mathbf{j} = \nabla \times \mathbf{B} \quad (34)$$

$$\nabla \cdot \mathbf{B} = 0 \quad (35)$$

where  $\mu = 4\pi \times 10^{-7}\text{kg m/C}^2$  is magnetic permeability of vacuum,  $\sigma$  is electrical conductivity of plasma.

### 2.1.3 Lagrangian formulation

The Lagrangian equations implemented in our codes result from a change of variables in the Eulerian equations described above into the Lagrangian coordinates. For example, in two-dimensional cylindrical geometry, the transformation of the derivatives

$$\frac{\partial}{\partial r}|_{z,t}, \quad \frac{\partial}{\partial z}|_{r,t}, \quad \frac{\partial}{\partial t}|_{z,r},$$

(where quantities to the lower right of the vertical bars are those that are held fixed), appearing in the Eulerian equations, are obtained using the Jacobian,

$$J = \frac{\partial(r, z, t)}{\partial(R, Z, t')} = \frac{\partial(r, z)}{\partial(R, Z)}$$

where we have used  $t' = t$ . The partial derivatives in the Eulerian equations can be written as

$$\frac{\partial}{\partial r}|_{z,t} = \frac{\partial(\cdot, z, t)}{\partial(r, z, t')} = \frac{\frac{\partial(\cdot, z, t)}{\partial(R, Z, t')}}{\frac{\partial(r, z, t)}{\partial(R, Z)}} = \frac{1}{J} \frac{\partial(\cdot, z)}{\partial(R, Z)}$$

Similarly,

$$\frac{\partial}{\partial z}|_{r,t} = \frac{1}{J} \frac{\partial(\cdot, r)}{\partial(R, Z)}$$

The time derivative becomes

$$\frac{\partial}{\partial t}|_{z,r} = \frac{1}{J} \frac{\partial(\cdot, r, z)}{\partial(t, R, Z)} = \frac{1}{J} \left[ \frac{\partial(r, z)}{\partial(R, Z)} \frac{\partial}{\partial t} - \frac{\partial(r, z)}{\partial(t, Z)} \frac{\partial}{\partial R} + \frac{\partial(r, z)}{\partial(t, R)} \frac{\partial}{\partial Z} \right]$$

Upon making the Lagrangian identification  $\partial R / \partial t = u$  and  $\partial Z / \partial t = v$ , we obtain

$$\frac{\partial}{\partial t}_{r,z} + \bar{\mathbf{U}} \cdot \nabla = \frac{\partial}{\partial t}|_{R,Z}$$

which expresses the relationship between the Eulerian and Lagrangian time derivatives with  $\bar{\mathbf{U}} = (u, v)$ .

#### 2.1.4 Boundary conditions in the current-sheet approximation

We have developed a set of fast routines for computation of flow regions where the sheet current approximation holds. This speedup results from the following physical considerations. Since the specific electrical conductivity of plasma with  $T_e \approx 10^2 \text{ eV}$  is of order of  $10^6 (\Omega m)^{-1}$ , the typical value of magnetic diffusivity  $\lambda \equiv (\mu \sigma)^{-1}$  is of order of  $1 \text{ m}^2/\text{s}$  which implies that in many physical setups of interest here the magnetic Reynolds number  $Re_m = VL/\lambda \gg 1$ . Indeed, for plasma flow with characteristic velocity of  $10^5 \text{ m/s}$  and characteristic length  $L$  of  $1 \text{ m}$ ,  $Re_m$  is of order of  $10^5$ . This means that only within limited regions where  $B$  changes significantly over a very short scale  $\delta$  the gradients are high

enough that the magnetic diffusion may not be safely neglected. In the rest of the flow, magnetic field lines are frozen in the plasma in a sense that all fluid particles remain on the field lines where they initially were.

Balancing the diffusion time  $\delta^2/\lambda$  and the convection time  $L/V$  results in the estimate  $\delta \propto L * Re_m^{-1/2}$  which means that  $\delta/L$  is of order of  $10^{-2}$  or less. In this case, plasma is magnetically confined by current in sheet layer of the width  $\delta$  which appears on the plasma boundary. This magnetically confined plasma has a free surface with no condition on the velocity component tangential to the boundary with vacuum. The normal velocity component  $v_n$  is equal to the normal velocity, if any, of the interface itself. The condition on the normal-to-the-boundary component of the magnetic field,  $B_n$ , requires that the change of  $B_n$  across the interface must be zero. On the other hand, if the plasma is considered as perfectly conducting, there may be discontinuities in tangential components of  $\mathbf{B}$ . The jump  $\Delta\mathbf{B}$  on the interface implies a surface sheet-current. By Stokes' theorem applied to equation (34), the sheet-current density per unit distance measured tangentially normal to the current is

$$\mathbf{J} = \frac{1}{\mu} \mathbf{n} \times \Delta\mathbf{B}, \quad (36)$$

$\mathbf{n}$  being a unit vector normal to the interface. Of course if plasma is considered as finitely conducting, the tangential field components must also be continuous across the interface. The extra condition of a zero  $\Delta\mathbf{B}$  matches the rise in the order of the field equation (33) when the magnetic diffusion term is included. The magnetic boundary layer of a finite thickness appears in this formulation. It can be viewed upon as a dilated version of a sheet-current made diffuse by the finite conductivity.

This magnetic field jump condition implies certain force balance at the plasma interface, namely, a discontinuity of pressure across the current sheet within which the normal  $\mathbf{j} \times \mathbf{B}$  force acts. Since the plasma is confined by its interface, the fluid acceleration is finite and the inertia term does not appear in the jump conditions. The magnetic force per unit volume consists of two terms:

$$\mathbf{j} \times \mathbf{B} = \frac{1}{\mu} (\nabla \times \mathbf{B}) \times \mathbf{B} = \frac{1}{\mu} ((\mathbf{B} \cdot \nabla) \mathbf{B} - \nabla B^2/2) \quad (37)$$

Inside the sheet-current, the first contribution  $(\mathbf{B} \cdot \nabla)\mathbf{B}/\mu$  is estimated as  $B^2/\mu R$  where  $R$  is the curvature radius of the interface. The second term  $\nabla B^2/2\mu$  is of order of  $B^2/\mu\delta$  and obviously dominates. Therefore, the force balance condition at the boundary is

$$\Delta(p + \mathbf{B}^2/2\mu) = 0, \quad (38)$$

where only the tangential components of  $\mathbf{B}$  contribute.

### 2.1.5 Plasma properties

We have developed an extensive database of material properties such as source terms for radiation transport and equations of state (EOS). The central issue in modeling of radiation transport is implementation of libraries of different models describing the emission and absorption of radiation which are required depending on the simulation under consideration. Local thermodynamic equilibrium (LTE) models are adequate for modeling radiation transport in the high-density colder regions plasmas while a full-LTE rate-equilibrium model is used to accurately model radiative processes in and around hot, lower-density, high-atomic-number plasmas. In many simulations, the coupling of the radiation to the fluid is treated explicitly. The energy removed from or deposited to the electrons by each energy group is summed over all energy bins transported for each computational zone. The source term is then explicitly added to the electron thermal energy equation. In some cases, however, the radiation and fluid are closely coupled and must be solved as such.

The analytic Thomas-Fermi/SESAME EOS was derived for use in instability simulations here. Tabular EOS's such as SESAME, while more accurate than the analytic EOS, have been found to result in excessive numerical noise during the simulation, to the extent of reaching high enough levels to render the entire simulation invalid. For the non-ideal gas EOS options, we have implemented a tabular look-up of the average  $z$  and average  $z^2$ . These tables are based upon information obtained from the 2000-group LTE opacity tables used in the radiation transport modules of our codes.

## 2.2 Numerical Implementation Aspects

### 2.2.1 Treatment of the Artificial Viscosity Term (AV)

The following general requirements were targeted for incorporation of the artificial viscosity in our code modules <sup>6,7</sup>:

- (1) Differential equations ( with a dissipative mechanism included ) should apply everywhere in the interior of flow, with no internal boundary condition required;
- (2) the basic conservation laws expressed by the Rankine-Hugoniot conditions should be obtained;
- (3) shocks should manifest themselves as approximate discontinuities in corresponding fields;
- (4) the thickness of a smeared shock should be independent of the shock strength and the material through which the shock travels;
- (5) the artificial viscosity should be independent of homogeneous expansions or contractions of the medium ( that is, in general, thermodynamically reversible processes should not give rise to shock formation);
- (6) the velocity component, parallel to the shock front in a medium, should be continuous;
- (7) angular momentum should be conserved; and
- (8) there should be no artificial viscosity for a velocity field under rigid rotation.

A number of different expressions have been developed and implemented into our multidimensional simulation codes. One of the best user options has the important feature of reducing to the Richtmyer and von Neumann form for one-dimensional flows for both two- and three-dimensional implementations:

$$\begin{aligned} AV &= a_o^2 \rho (\delta v)^2, \delta v < 0; \\ AV &= 0, \delta v \geq 0. \end{aligned} \tag{39}$$

Here  $\rho$  is the fluid density,  $\delta v$  is the change in velocity across a zone, and  $a_o$  is a constant

related to the number of computational mesh points over which the shock is smeared. This form of  $AV$  satisfies most of the desired properties. In particular, Condition 2 is satisfied, provided the dimensions over which the shock is smeared are small compared to other dimensions.

### 2.2.2 Numerical Treatment of Boundary Conditions

The treatment of boundary conditions for the hydrodynamics in our Lagrangian code modules is accomplished without any special treatment of the momentum equation at the boundary. Nonrigid boundaries are treated by assuming the pressure is zero (or prescribed) in the region outside the computational mesh.

The proper boundary condition for thermal-energy diffusion is the zero gradient (“no flux”) boundary condition at a vacuum-fluid interface. To accommodate this no-flux condition, it is necessary to extend the computational grid when computing temperature gradients near a vacuum interface (“ghost cell”). The ghost cells are used only to enforce the boundary condition and do not affect material zones in the problem. At slip surfaces, the zero-temperature gradient condition is also implemented.

### 2.2.3 Thermal flux limitation

It has been shown by a number of authors that the Spitzer-Harm electron thermal conductivity<sup>12</sup> used in most high-energy-density simulations breaks down under two conditions. The first is at initial low “room” temperature and normal density where the Spitzer-Harm conductivity will result in low values. The second is in regions where the electron mean free path is large compared to the thermal-gradient scale length. In the latter case Fourier’s law for thermal conduction is invalid. In this work, we followed the existing practice in high-energy-density plasma simulation research to limit the thermal flux to a maximum value corresponding to the energy transported by free-streaming particle flow<sup>13</sup>. There are two methods commonly used for this limiting procedure. In both cases an effective free-streaming conductivity is found by dividing the free-streaming flux by the temperature

gradient. In the first case the conductivity used in the conduction equations is set equal to the minimum value between the Spitzer-Harm thermal conductivity and the effective free-streaming conductivity. The second method is to use a harmonic mean between the two conductivities, thereby allowing for a smooth transition between the thermal conduction given by Spitzer-Harm and the free-streaming value. The application of a flux limiter, while physically motivated, is *ad hoc*. The use of flux limiters results in approximately physically correct behavior.

## 2.2.4 Grid distortion control and rezoning techniques

A number of algorithms have been implemented in our code modules in order to minimize the development of nonphysical grid distortions. For both the two- and three- dimensions options, the tensor artificial viscosity of stabilizing grids similar to that developed by Wilkins <sup>9</sup> has been implemented. In the two-dimensional modules, an additional grid-distortion-control option has been implemented based on a rotational artificial viscosity originally developed for the tensor code <sup>10</sup>.

It should be mentioned that rezoning of one-, two- and three-dimensional Lagrangian hydrodynamics programs is becoming an important area of research in code development in the high-energy-density plasma simulation field. Rezoning represents the Eulerian step associated with the arbitrary Lagrangian/Eulerian implementation of the hydrodynamics routines in RIGEL. During this phase of the simulation the computational mesh can be rezoned (either in a fully Eulerian manner or by some other procedure) and all advective flux calculations are performed. When flow distortions occur that result in unacceptably small time steps or poor resolution in regions of interest, some corrective action is required. In our code modules, we use several rezoning algorithms, including van Leer's methods <sup>14-16</sup>. Donor-cell differencing has been implemented for the one-, two-, and three- dimensional options.

### 2.2.5 Technical aspects of solver implementation

Here we illustrate some issues and methods used in discretization, solvers, and parallel implementation. Consider for example the energy diffusion in two dimensions on a distorted mesh which also includes the effects of heat flow from the "corner" zones. Corner zones are defined as those surrounding the zone of interest but not directly adjacent (sharing a common interface) to that zone. The method used in this work builds upon our algorithm previously developed for the ORCHID code and consists of a combination of both finite difference and methods more closely related to finite elements<sup>11</sup>. Let us designate the temperature at the intersection point of branch line  $j$ , zone  $i$ , as  $T_{b_j}^i$ . Let also  $T_{c_k}$  designate the temperature defined at the area centroid of zone  $k$  so that, say, the temperature at vertex point 1 is obtained by averaging of centroid temperatures

$$T_{v_1} = \frac{T_{c_1} + T_{c_2} + T_{c_3} + T_{c_4}}{4}$$

Approximation of the temperature gradient involves the following length scales:  $\lambda$  is the length of the panel from vertex point 1 to point 2,  $\lambda_1$  is the length along the panel from vertex point 1 to the intersection point of the normal to the panel from the area centroid of zone 1;  $\lambda_2$  is the length along the panel from vertex point 1 to the intersection point of the normal to the panel from the area centroid of zone 2;  $\Delta x_{1,2}^i$  are the normal distances from the branch line intersection points in zones 1,2 to the panel, respectively.

The form of the temperature gradients depends upon which branch lines the panel perpendicular bisector intersects. The expressions for temperature gradient for the four possible cases follow:

(a) For  $\lambda_1 < \lambda/2$  and  $\lambda_2 < \lambda/2$ ,

$$\Delta x_1^1 = \frac{x_1(\lambda/2)}{\lambda - \lambda_1}, \quad \Delta x_2^1 = \frac{x_2(\lambda/2)}{\lambda - \lambda_2}, \quad T_{b_1}^1 = \frac{(\lambda/2 - \lambda_1)T_{v_2} + (\lambda/2)T_{c_1}}{\lambda - \lambda_1},$$



$$T_{b_2}^1 = \frac{(\lambda/2 - \lambda_2)T_{v_2} + (\lambda/2)T_{c_2}}{\lambda - \lambda_2}, \quad \nabla T = \frac{(T_{b_2}^1 - T_{b_1}^1)}{\Delta x_2^1 + \Delta x_1^1}.$$

(b) For  $\lambda_1 > \lambda/2$  and  $\lambda_2 > \lambda/2$ ,

$$\Delta x_1^2 = \frac{x_1(\lambda/2)}{\lambda_1}, \quad \Delta x_2^2 = \frac{x_2(\lambda/2)}{\lambda_2}, \quad T_{b_1}^2 = \frac{(\lambda_1 - \lambda/2)T_{v_2} + (\lambda/2)T_{c_1}}{\lambda_1},$$

$$T_{b_2}^2 = \frac{(\lambda_2 - \lambda/2)T_{v_1} + (\lambda/2)T_{c_2}}{\lambda_2}, \quad \text{then} \quad \nabla T = \frac{(T_{b_2}^2 - T_{b_1}^2)}{\Delta x_2^2 + \Delta x_1^2}.$$

The two other possible cases are

(c)  $\lambda_1 > \lambda/2$  and  $\lambda_2 < \lambda/2$ ,

(d)  $\lambda_1 < \lambda/2$  and  $\lambda_2 > \lambda/2$ .

Similar derivation using the correct form of intersection point temperature and the normal from the intersection point to the panel yields the expressions for the temperature gradient for these final two cases:

$$(c) \quad \nabla T = \frac{(T_{b_2}^1 - T_{b_1}^2)}{\Delta x_2^1 + \Delta x_1^2},$$

$$(d) \quad \nabla T = \frac{(T_{b_2}^2 - T_{b_1}^1)}{\Delta x_1^2 + \Delta x_1^1}.$$

Although the temperature gradient still retains the simple form  $\Delta T/\Delta x$  it is nonlocal and accounts for both grid distortion and the influence of surrounding "corner" zones. This procedure results in a sparse matrix which is inverted using the successive over-relaxation (SOR) variation of the Gauss-Seidel method. Consider a set of  $m$  linear algebraic equations, written in matrix form as

$$I - L - U = b,$$

where  $I$  is the unit (identity) matrix of order  $m$  and  $L$  and  $U$  represent lower and upper null triangular matrices, respectively

$$-L = \begin{pmatrix} 0 & 0 & 0 & 0 \\ a_{2,1} & 0 & 0 & 0 \\ a_{3,1} & a_{3,2} & 0 & 0 \\ a_{m,1} & a_{m,2} & a_{m,m-1} & 0 \end{pmatrix}$$

$$-U = \begin{pmatrix} 0 & a_{1,2} & a_{1,3} & a_{1,m} \\ 0 & 0 & a_{2,3} & a_{2,m} \\ & & & a_{m-1,m} \\ 0 & 0 & 0 & 0 \end{pmatrix}$$

Using  $L$  and  $U$ , the iteration scheme is

$$x^{n+1} = x^n + \omega(Lx^{n+1} + Ux^n + b - x^n),$$

where the superscript denotes the iteration number. The change in  $x$  between two iterations ( $x^{n+1} - x^n$ ) is referred to as the correction to  $x$  or the displacement vector. The relaxation parameter  $\omega$  is usually a real positive number between 0 and 2.0. For  $\omega$  less than 1 the method termed is "under-relaxed". Note that  $\omega = 1$  reduces the SOR iteration to Gauss-Seidel iterates.

Both the Gauss-Seidel and SOR methods replace  $x^n$  by  $x^{n+1}$  as soon as  $x^{n+1}$  becomes available. SOR is performed using a relative error convergence criterion:  $(x^{n+1} - x^n)/x^n \leq \epsilon$ , where  $\epsilon$  is chosen typically in the range  $10^{-8}$  to  $10^{-6}$  depending on the problem.

On standard single to "few" central-processor implementations we have implemented SOR based on the Gauss-Seidel iteration procedure whereupon determining and updating

iterate it is used in succeeding calculations of other iterates. For a "many"- processor implementation there is an option for a Jacobi-type iteration where the iterates are updated only at the end of the overall system-iteration step (sweep). This solution procedure, while easier to implement on a many-processor computer system, represents an area of further research and development. The procedures of determination of the gradient on a distorted mesh in two dimensions and three dimensions are similar. In three dimensions, instead of intersections of the panel normal with linear interpolation segments between nodal points and zone centroids, intersections with interface normal and planes is used, resulting in a 27 diagonal system.

The current version of ELPIC-MHD includes parallelization options which force the most time-consuming internal loops of the code run in parallel on many processors. The advantage of using a parallel code becomes apparent taking into account that 95 percent or more of the entire CPU time in computation of the magnetic field is consumed by the inner nested loops which implements Gauss-Seidel algorithm with overrelaxation (SOR). In this loop, the central processor recalculates full arrays of values of the magnetic field component along with the current local iteration residual matrix  $R$  as well as the average residual for the entire matrix. At each time step, up to several thousands of system-iteration sweeps may be required for each of the magnetic field components. On a single processor this procedure routinely takes at least 70-80% of the total CPU time on large grids of practical interest.

In the hydrodynamical part of the code, transfer of Lagrangian particles takes 60 to 75% of the rest of the CPU time. The core part of this procedure is coded as a loop of about 600 executable statements which consumes almost 100% of the total particle-pushing CPU time. This loop is executed once for each one of the Lagrangian particles.

Together, these two loops take 90 to over 95% of the total CPU time. Therefore, the maximum acceleration by as much as 15-20 can be achieved by optimal parallelization of only these two loops on 20-30 processors. Parallelization of the Lagrangian stage is straightforward. For a "few" processors, the most efficient approach is to use the par-

allelization directives at the source level. Source-independent parallelization algorithms have been found to split the loops in such a way that particle pushing affects distant elements of the corresponding Eulerian grids, automatically providing a high efficiency of such parallelization.

The bottleneck of speedup due to optimization of the Eulerian stage using source-level directives is efficient treatment of second order differential operators. The stencil here involves several elements, some of which result from calculation using the same formula obtained earlier in the nested loop. This dependency is required to take advantage of overrelaxation formula which helps to dramatically reduce the total number of iterations. Full explicit parallelization of this stage, performed using source-level directives which divide loops into several parts and force the processors to execute those parts in parallel, is not efficient. The reason is that the processors have to wait until the values of the function along the adjacent subdomains are calculated by the neighboring processors.

An alternative parallelization strategy provides almost linear scaling of performance with the number of processors. The idea here is as follows. Convergence criteria outside the stencil at given point in the computational domain are always known while the operations at this given point are performed. At the same time, at least dozens of sweeps are performed over the same array within a time step. The optimized algorithm scans the array line-by-line starting from the line next to the domain boundary. After scanning of three lines is completed by the first processor, the same loop starts on the second processor which begins scanning again from the first line. The array elements read and written by the second processor are fully independent of the elements read and written by the first one, since the calculated elements are separated by at least two lines of the array. Computational stencils involved in reading and writing operations do not overlap. Therefore, two consequent internal iterations are performed in parallel by two individual processors with virtually no overhead. When the second processor completes calculation of the first three lines, the third processor takes up the job beginning with the first line and so on. When the first processor completes execution of the last line of the matrix, it checks whether the last

processor has completed execution of the first three lines and if this condition is met it starts scanning the first line again. All the other processors follow the same algorithm. After a preset number of full sweeps, one of the processors (in our implementation, the last one) checks the overall convergence criteria for the entire matrix using the lower estimate of the residual norm which it accumulated during the last sweep (the real residual norm can only be less). If the norm does not exceed the known (preset or calculated) value, the loop execution is completed.

In this way, using up to  $N/3 - 1$  processors where  $N$  is the total number of lines result in minimal degradation of relative performance. This cyclic algorithm provides almost linear scaling if the required total number of loops is much greater than the number of available processors. Using the limited depth multigrid method improves performance even further. If the number of multigrid levels is limited by two, the algorithm is identical to the one described above, with the only difference that the number of processors which can be effectively used in parallel may not exceed  $M/3-1$ , where  $M$  is the number of lines in the coarser subgrid.

In simulations involving "very many" processors, the arrays containing particle data have to be sorted out so that particles from consequent elements of these arrays always belong to the cells of Eulerian grid separated by at least two other cells. For three-dimensional grids this critical number of processors is about  $(1/3)^3 \approx 1/30$  of the total number of Eulerian cells which ranges from tens of thousand to millions depending upon the application.

## Chapter 3

# Numerical Modeling of Plasma Devices

Our computational strategies described in the previous chapter can be applied to a wide variety of practically important issues such as

- advanced weapons systems;
- pulsed plasma radiation sources;
- advanced propulsion systems, including prospective space-application thrusters based on burning of  $D - He^3$ , e.g. nuclear thermal propulsion thrusters;
- microwave generation;
- inertial confinement fusion.

In this chapter we review several prototype simulations of high energy density plasma devices of interest for the AirForce, emphasizing plasma focusing and energy conversion. These test cases are representative of a variety of parametric studies that we performed in the course of this project, including variable device geometries, physical/material properties, boundary/initial conditions, different code modeling modules options used, etc.

The first test case presented here involves a prototype configuration of a plasma beam compression device used for pulse magnetic field confinement of injected plasma beams. In this device, compression is due to the configuration of magnetic field in the vacuum chamber

of nearly-conical shape. The device responsible for generation of short pulse magnetic field is located outside our computational domain. The initial and boundary conditions in the runs illustrated in Figs 1-18 correspond to relatively cool fully ionized homogeneous plasma with a uniform coefficient of ionization injected through the inlet located on the right side of each plot. The beam is formed and pre-conditioned during homogenization, acceleration, and preliminary compression stages. The injection speed used in presented runs is 50 km/s (the entire range of injection speeds from 10 to 150 km/s has been studied). The inlet plasma density in the beam drops sharply from a typical value of  $0.03 \text{ Kg/m}^3$  in the core to very small values outside of a tube of about 75% of the overall inlet radius. Most of the magnetic flux injected through the inlet is concentrated in the area of low plasma density restricted on the outside by the inner surface of the device wall. The magnetic flux is set constant over duration of plasma injection. The integral magnetic fluxes through the inlet and through the outlet (located on the left side of our plots) are equal.

Since the injected beam is confined by magnetic field, dense plasma is isolated from the outer wall. The possibility to set the tangential component of particle velocity at the wall to zero is embedded in our code modules in order to properly model wall boundary layer effects important for device efficiency and durability analysis.

This magnetically confined plasma beam propagates through the chamber with smoothly diminishing cross-section and increasing density. Our setup allows for a parametric study of the behavior of this magnetically confined and compressed plasma, thus prototyping a practically important experimental study aimed at achieving maximum density in the plasma jet near the outlet accompanied by maximum acceleration/inhibited deceleration and therefore avoiding inasmuch as possible conversion of the kinetic energy into heat. This optimization is important in several applications which involve an outcoming jet hitting a target in order to generate x-rays pulses of desired characteristics with maximum intensity.

In Figs. 1-7 we show a complete time history of a run in which the magnetic field configuration is near the optimum from the point of view of above considerations. In Fig. 1 we plot the initial setup with the magnetic field lines plotted in green color.

Initially the chamber is nearly empty. A highly conducting plasma beam is injected through the inlet on the right side of the picture. The specific internal energy of different plasma regions is shown in terms of a color palette imitating those of a heated body. Dark grey color stays for cold material, whereas shades of red transforming into yellow, then green, blue, and at last white indicate increasing energy and temperature. The color scale on top of Fig. 1 shows the color-energy correspondence. For convenience, the specific internal energy is expressed in degrees Kelvin.

In the lower part of Fig. 1, we plot the very beginning of plasma compression. The effective magnetic field pressure applied to the plasma surface generates a shock wave. At the same time, the front axial part of the beam does not experience any significant magnetic pressure and tends to slightly expand and cool down.

The compression history is shown in Fig. 2. The compression shock at the surface which is initially strong is partly relieved by a slight expansion of the frontal surface of the beam. This expansion is faster in the core area where the effective magnetic pressure is minimal, producing a clearly visible distortion of the frontal surface of the plasma beam (which was initially set flat).

In Fig. 3 we show the most interesting stage of the compression process, the focusing. In the bottom part of Fig. 3, the very moment of focusing is shown. Shortly before the focusing event, the surface shock reconnects along the entire plasma surface. The bright spot shows the exact position of the focal point. Until the very moment of focusing the plasma velocity slowly decreases, but right after the focusing the plasma beam tip on the left side of the focal point starts to accelerate.

In Fig. 4 we plot developing hot area in the beam core produced by collapse of the imploding shocks on the axis, resembling that in Munro jets. The velocity of forming axial hot and dense jet is always directed against the mean flow velocity. Therefore, the kinetic energy of the initial plasma beam is partly converted into heat and tends to slow down the bulk flow. Excessive core heating poses a limitation on the maximum compression rates that can be achieved.



In Fig. 5 one can see formation of a metastable structure in the focused plasma beam which consists of a sequence of domains with lower or greater thickness. The cause is clearly visible in the top part of Fig. 5: two consequent axial jets are formed, both slowing down the compressed beam.

In Fig. 6, we plot a developed axial jet that has propagated far upstream, progressively slowing down the beam. The maxima of compression ratio, temperature, and pressure, as well as the velocity minimum are achieved in the area adjacent to the outlet, where plasma effectively expels the magnetic field from the channel. The configuration shown in the bottom portion of Fig. 5 precedes a moment when substantial number of particles reach the wall blocking the way to the magnetic flux.

This blocked configuration is shown in Fig. 7. In real life laboratory experiment this stage corresponds to magnetic field being completely expelled from the chamber so that its energy is almost instantly emitted in form of electromagnetic waves. Most of the kinetic energy of our initially cold incoming jet is immediately converted into shock heating of the stagnated dense plasma cloud near the outlet, in the leftmost part of the chamber (bright white color which depicts temperatures in the Kev range). A magnified part of the stagnation zone is shown in the bottom portion of Fig. 7. A very hot rarefied plasma region appears as separate particles and propagates far upstream in the gap between the jet and the wall. These small portions of plasma merge back with the surface of the core jet and substantially heat up the thin surface layer.

In Fig. 8 we show a configuration corresponding to the same initial and boundary condition of the flow, with a magnetic field approximately twice as high as in previous run. A naive assumption would be that increased magnetic field should lead to increased beam compression and therefore improved efficiency.

However, data plotted in Fig. 8 indicates that such naive assumptions can be wrong. Indeed, in this run a stronger magnetic field initially makes the first focal point closer to the inlet and formes a thinner, denser compressed jet. This jet then accelerates to a slightly higher velocity. However, the rarefied and fastest leftmost edge of the jet experiences rapid

deceleration by the magnetic field. This creates a shock at the jet tip, overheats it and makes it rapidly expand. This in turn forms a cavity-like configuration of the magnetic field, leading to further increase of plasma deceleration. This positive feedback instability leads to rapid formation of a dense hot stagnated plasma cloud. The kinetic energy is lost into heat and emitted prematurely inside the chamber. This result strongly indicates that optimum plasma focusing can be achieved within nontrivial parameter regimes which elude common sense but require systematic numerical study.

In Figs. 9 - 13, we plot a time history of another run characterized by near-the-optimum magnetic field magnitude. In these Figures, walls and magnetic field lines are not shown. This simulation intentionally starts from a domain already filled with moving plasma, except for a small two cell-wide gap between the plasma and wall. The goal is to computationally determine the minimum magnitude of the magnetic field which separates dense plasma from the wall before it blocks the magnetic flux. Fig. 10 shows the plasma configuration at such magnetic field. This is a nearly ideal focusing. Figs. 11 - 13 show the rest of the numerical experiment. Initially (Fig. 11) the jet diverges after the focal point. At a later time (Fig. 12), the plasma touches the wall forming a strong shock. At last (Fig. 13) the stagnation cloud blocks the channel near the outlet.

In Fig. 14 we show the outcome of a run with the same initial configuration but an even lower magnitude of magnetic field. Here, we plot the walls but not the magnetic field which is concentrated in the gap next to the wall and within it. In this experiment, no focal point appears at all. Shortly after the start, plasma contacts the wall forming a shock that separates far from the outlet. The shock collapses onto the axis and forms a stagnation core which then absorbs and converts all the jet kinetic energy. Fig. 14 illustrates the instant of stagnation core formation.

We have seen that the parameter domain corresponding to absence of premature chamber blocking can be multiconnected. In Figs. 15 - 18 we plot a time history of a run with the magnetic field amplitude just slightly stronger than the optimum (c.f. with the series shown in Fig. 8 which corresponds to only slightly lower magnetic field). The configuration

shortly after the start is shown in Fig. 15. As one can see from Figs. 16-18, a dense jet with a sequence of focal points forms and exists for an extended time. Comparing Figs. 17 and 18, one can see that the first focal point retains its position during the run while the second focal point slowly moves upstream, away from the outlet.

Special attention was given throughout the project to the problem of compact toroid acceleration by magnetic field. The compact toroid is a nearly force-free plasma configuration whose acceleration is provided by a pulse of toroidal magnetic flux injected radially inwards. This pulse also forces reconnection of magnetic field lines to form a closed toroidal plasma-field object with extended lifetime.

A set of specialized subroutines has been specifically developed in order to fast set up nearly force-free toroidal configuration in complex device geometries. In Figs. 19 - 22 we plot the acceleration stage of compact toroid in a prototype device similar to the formation and compression regions of the MARAUDER facility. In Fig. 19 we plot the stable flow/magnetic field configuration as created by our specialized setup routine. The formation region of the prototype device has constant width and the narrowing zone corresponds to the compression region. A nearly round cross-section of the compact toroid is located next to one of the inlets designed for injection of a pulse acceleration flux. In a real device, this corresponds to the zone near the muzzle of the formation gun. A blowup of the outside cross section of the magnetic field configuration calculated by fast solver is plotted in Fig. 20. Inside the toroid, equilibrium distribution based upon balance of magnetic and hydro pressure is computed. Temperature, density and hydro pressure smoothly increase towards the axis of the toroid, compensated by the magnetic effective pressure gradient. The total toroid mass is  $0.72 \times 10^{-3}$  grams. The total initial number of computational Lagrangian particles in the toroid is 205,000. Since the particles breed in the areas of high stretching, their number increases during the run.

The configuration at a later time is shown in Fig. 21. The magnetic field around the toroid has significantly changed. Notice high field gradients near the rear surface of the toroid. The magnetic force acting at the rear surface is now much above that at the front

surface, providing for the acceleration force.

A representative later stage of the toroid evolution dynamics is plotted in Fig. 22. The magnetic field is not confined within the toroid – field lines leave the plasma region and then return back in the toroid body. The development of small scale surface structures is due to the weak instabilities. Significant reconfiguration of the internal field in the compact toroid region is due to the external accelerating field which is intentionally chosen comparable to the internal field. Optimization search for non-destructive threshold ratio of the internal to external field is an important problem for compact torus accelerator design which can be studied using our numerical techniques.

## References

1. J. A. Shercliff, A Textbook of Magnetohydrodynamics, Pergamon Press, 1965.
2. Kenro Miyamoto, Plasma Physics for Nuclear Fusion, The MIT Press, Cambridge, Mass.
3. N. A. Krall and A. W. Trivelpiece, Principles of Plasma Physics, McGraw-Hill, New York, 1973.
4. A. I. Akhiezer, I. A. Akhiezer, R. V. Polovin, A. G. Sitenko, and K. N. Stepanov, Plasma Electrodynamics, Pergamon Press, Oxford, 1975.
5. L. Spitzer, Jr, Physics of Fully Ionized Gases, Wiley Interscience, New York, 1962.
6. J. VonNeumann and R. D. Richtmyer, J. Appl. Phys. 21, 232 (1950).
7. W. D. Shultz, in *Methods in Computational Physics*, eds. B. Alder, S. Fernback, and M. Rotenberg (Academic Press, New York, 1964), Vol. 3, p. 1-45.
8. M. L. Wilkins, in *Methods in Computation Physics*, eds. B. Adler, S. Fernback, and M. Rotenberg (Academic Press, New York, 1964) Vol. 3, p. 211-263.
9. M. L. Wilkins, R. E. Blum, E. Cronshesen, and P. Grantham, Lawrence Livermore National laboratory Report, UCRL-51574 (1975).
10. G. Maenchen and S. Sack, in *Methods in Computational Physics*, eds. B. Adler, S. Fernback, and M. Rotenberg (Academic Press, New York, 1964), Vol. 3, p. 181-210.
11. R. L. McCrory and C. P. Verdon, in *Computer Applications in Plasma Sciences and Engineering*, ed. A. Drobot, (Springer-Verlag, New York, 1991), p. 291-325.
12. L. Spitzer, Jr. and R. Harm, Phys. Rev. 89, 977 (1953).
13. R. C. Malone, R. L. McCrory, and R. L. Morse, Phys. Rev. Lett. 34, 721 (1975).
14. B. van Leer, J. Comput. Phys. 23, 263, (1977).
15. B. van Leer, J. Comput. Phys. 23, 276, (1977).
16. B. van Leer, J. Comput. Phys. 32, 101, (1979).

# List of Figures

Fig. 1. The initial setup of a prototypical plasma beam compressing device. Bottom portion: initial stages of plasma beam injection and compression. Surface compression shocks are shown.

Fig. 2. Compression process by JxB forces applied to the surface of injected plasma beam. Faster expansion of plasma at the front surface of the beam.

Fig. 3. Plasma beam focusing at the point of maximum compression (the "focal point"). Top: a moment before the focusing; bottom: the focusing instant.

Fig. 4. Top portion: the fastest core part of the focused plasma beam leaves the chamber and hits a target located beyond the computational domain. Bottom portion: formation of two consequent temperature maxima near the beam axis.

Fig. 5. A metastable fine structure of the beam characterized by two focal points and two maxima in density and temperature at the axis is formed with the second maximum located near the outlet.

Fig. 6. Expansion of the beam portion near the outlet due to pressure increase induced by the beam slowdown. The kinetic energy conversion into heat causes pressure increase and beam expansion which is most apparent near the outlet. This expansion narrows the channel of the magnetic flux and increases magnetic pressure near the outlet which accelerates the beam slowdown.

Fig. 7. The gap between the plasma and the wall collapsed and magnetic field is expelled from the internal volume of the chamber. Bottom: a blowup of the near outlet zone at the same time instant as shown at the top. A strong shock propagates upstream converting

nearly all the plasma beam kinetic energy in the chamber into heat.

Fig. 8. Increased magnitude of the magnetic field as leading to premature stagnation of the plasma cloud near the outlet. Stagnation is caused by fast expansion of the plasma beam tip due to increased rate of slowdown.

Fig. 9. A configuration used to detect the threshold magnitude of the magnetic field which forces the nearly-optimum plasma beam to focus. Moving plasma initially fills the entire chamber, leaving only a narrow gap for the magnetic field. The threshold magnetic field prevents plasma-wall contact which would otherwise create a very strong shock.

Fig. 10. The same run: a moment of nearly optimum focusing. A bright spot on the plasma beam surface closer to the inlet is a trace of a marginally short contact between the plasma and the wall. The perturbation caused by such contact is still capable of relaxing numerically; a very small relative reduction of the magnetic field magnitude causes rapid development of the strong shock and destruction of the beam.

Fig. 11. The same run: the beam past the focal point diverges after focusing.

Fig. 12. The same run: formation of a stagnated area near the outlet shortly after the diverging part of the beam touches the wall.

Fig. 13. The fully developed structure of stagnated dense hot low-velocity plasma cloud near outlet. This moment determines a "natural lifetime" of the magnetically focused plasma beam. However, the focusing device efficiency degrades rapidly starting from the first implosion of the shock on the axis shown in the previous Figure.

Fig. 14. The plasma beam structure corresponding to a below-than-threshold magnetic field magnitude. A sequence of weak shocks collapsing onto the axis results in merge and amplification and, shortly after, in formation of shock of extreme amplitude which forces the total stagnation.

Fig. 15. The early stage of the run with magnetic field much stronger than the threshold.

Fig. 16. The same run: a moment before the compressed beam leaves the chamber through outlet. The first focal point is unusually close to the inlet.

Fig. 17. The same run: a moment of formation of the second focal point between the

first one and the outlet.

Fig. 18. The same run: formation of the third focal point next to the outlet. By this time, kinetic energy losses in the beam are still negligibly small. In this run the lifetime of the compressed dense beam is even longer than in the runs shown in Figs. 1-7 and 9-13.

Fig. 19. A compact toroid in prototype accelerator device simulated using 205,000 particles, each one representing an individual Lagrangian portion of plasma - a complex object which can develop, change shape and internal density and breed under certain conditions - form the initial body of the toroid.

Fig. 20. A magnified area around the toroid shortly after the accelerating toroidal magnetic flux has been injected radially inward through the inlet above.

Fig. 21. The flow/field configuration during the acceleration stage. Magnetic field lines leaving the interim of the toroid and embedded in it are plotted along with the flow structures developing at the surface. Although the embedded field is visibly distorted, the overall structure is stable.



28	140	364	700	1149	1682	2354	3139	4009	4990
84	252	504	897	1401	2018	2719	3560	4485	

\*1.0E+02

O u t l e t

Magnetic field

Time 0  $\mu$ s

Injected plasma

Time 1  $\mu$ s

Fig. 1

Compression shock

Time 10  $\mu$ s

Time 15  $\mu$ s

Fig. 2



Time 25  $\mu$ s

Time 30  $\mu$ s

Fig. 3



Time 40  $\mu$ s



Time 50  $\mu$ s

Fig. 4

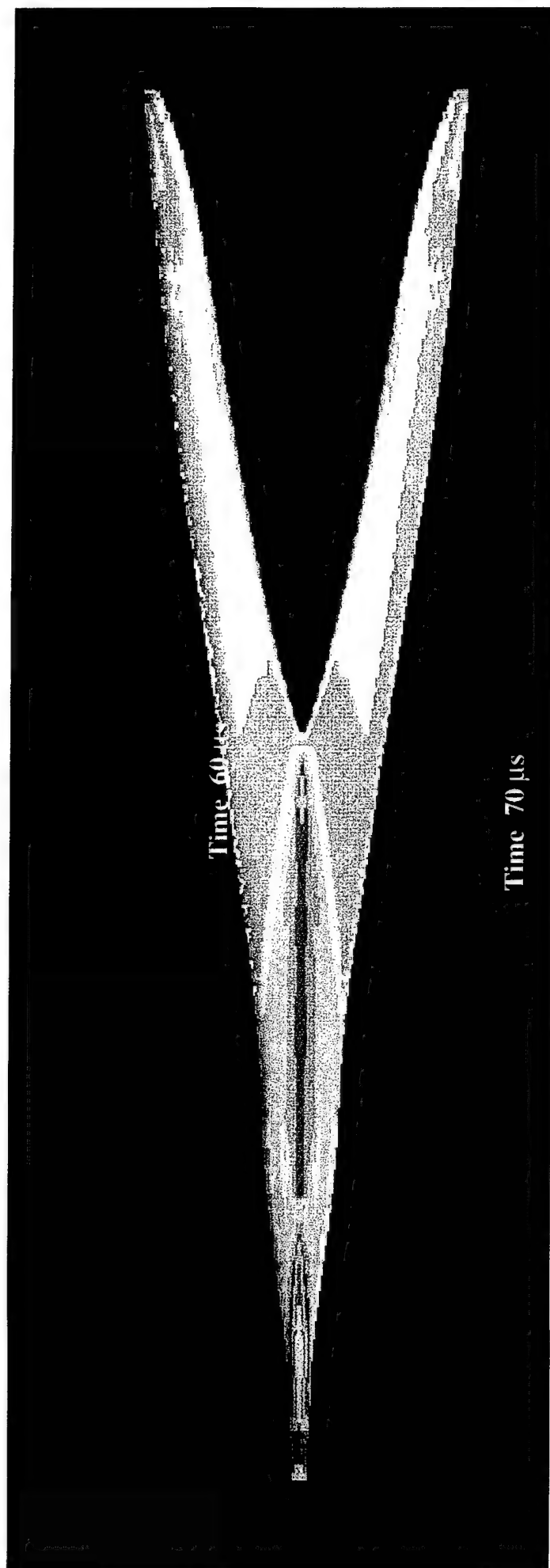
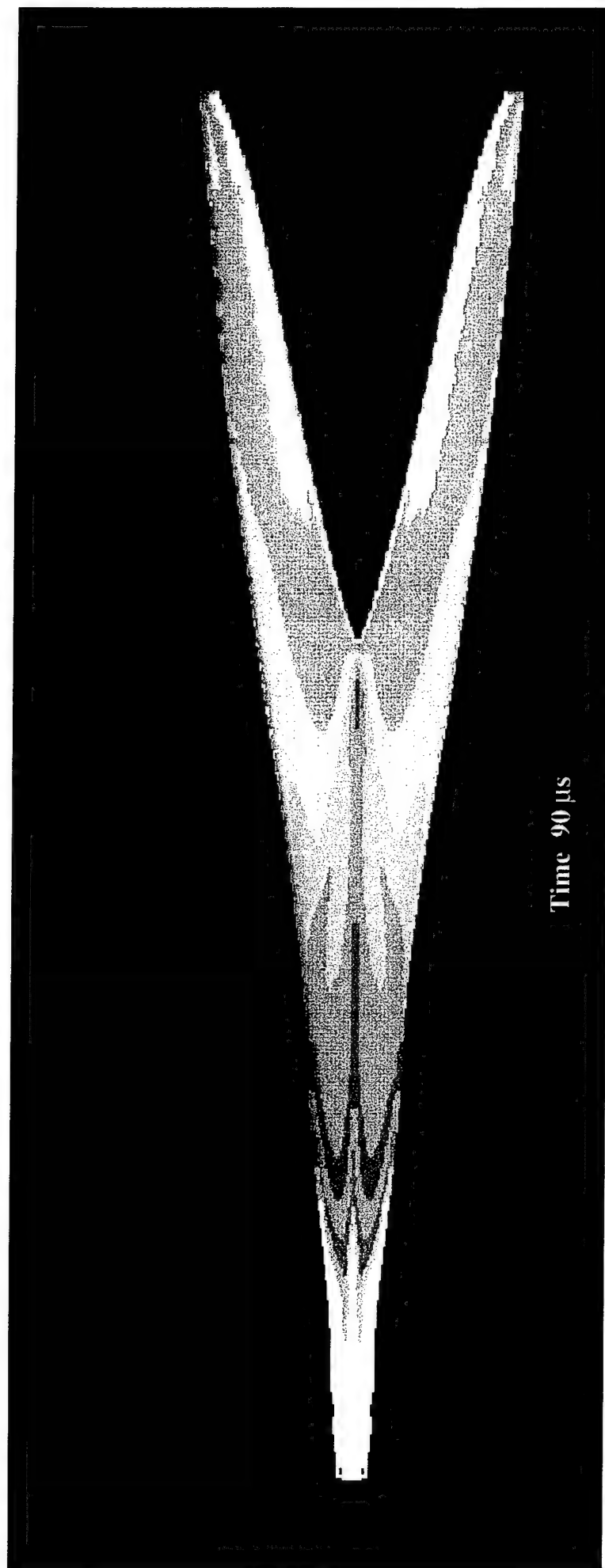
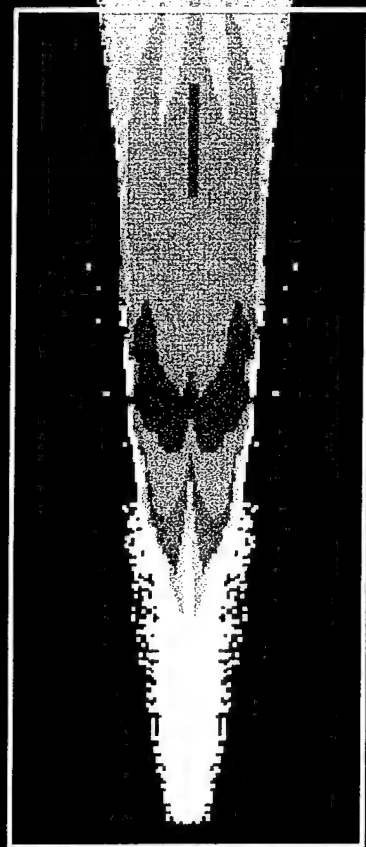


Fig. 5



**Fig. 6**

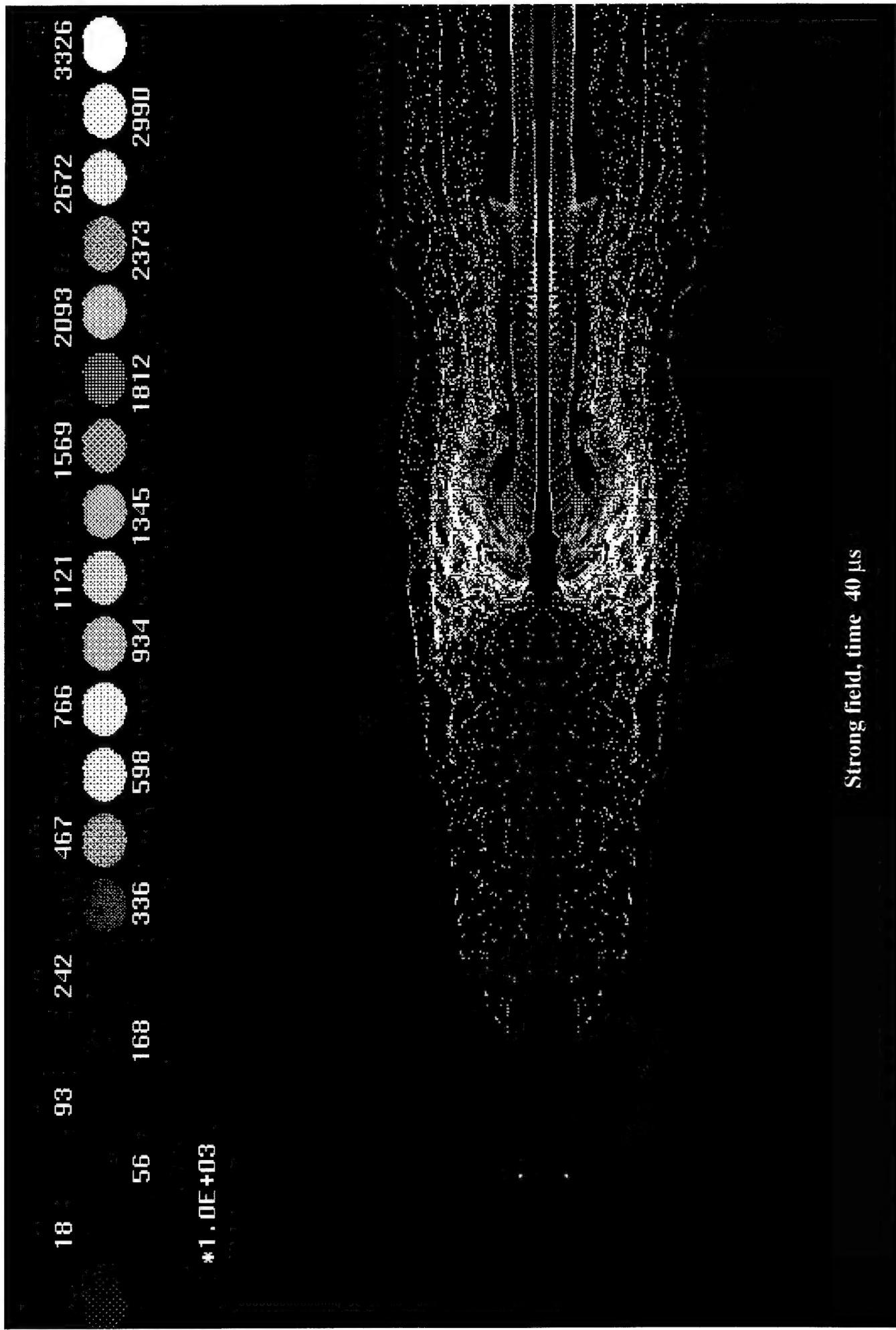


Time 100  $\mu$ s



Time 100  $\mu$ s (magnified)

**Fig. 7**



Strong field, time 40  $\mu$ s

Fig. 8



Cool plasma with  
uniform density



**Fig. 9**

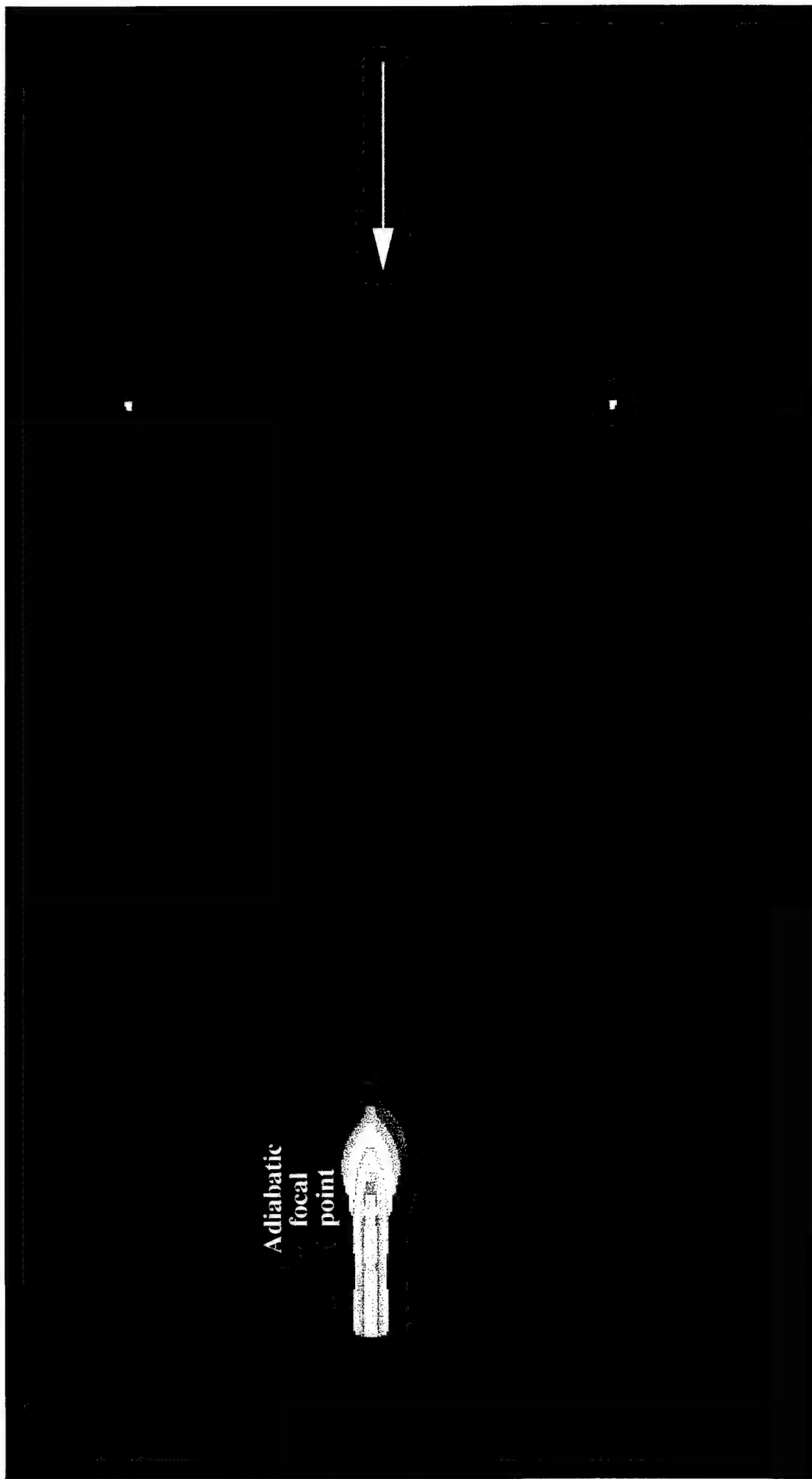


**Fig. 10**

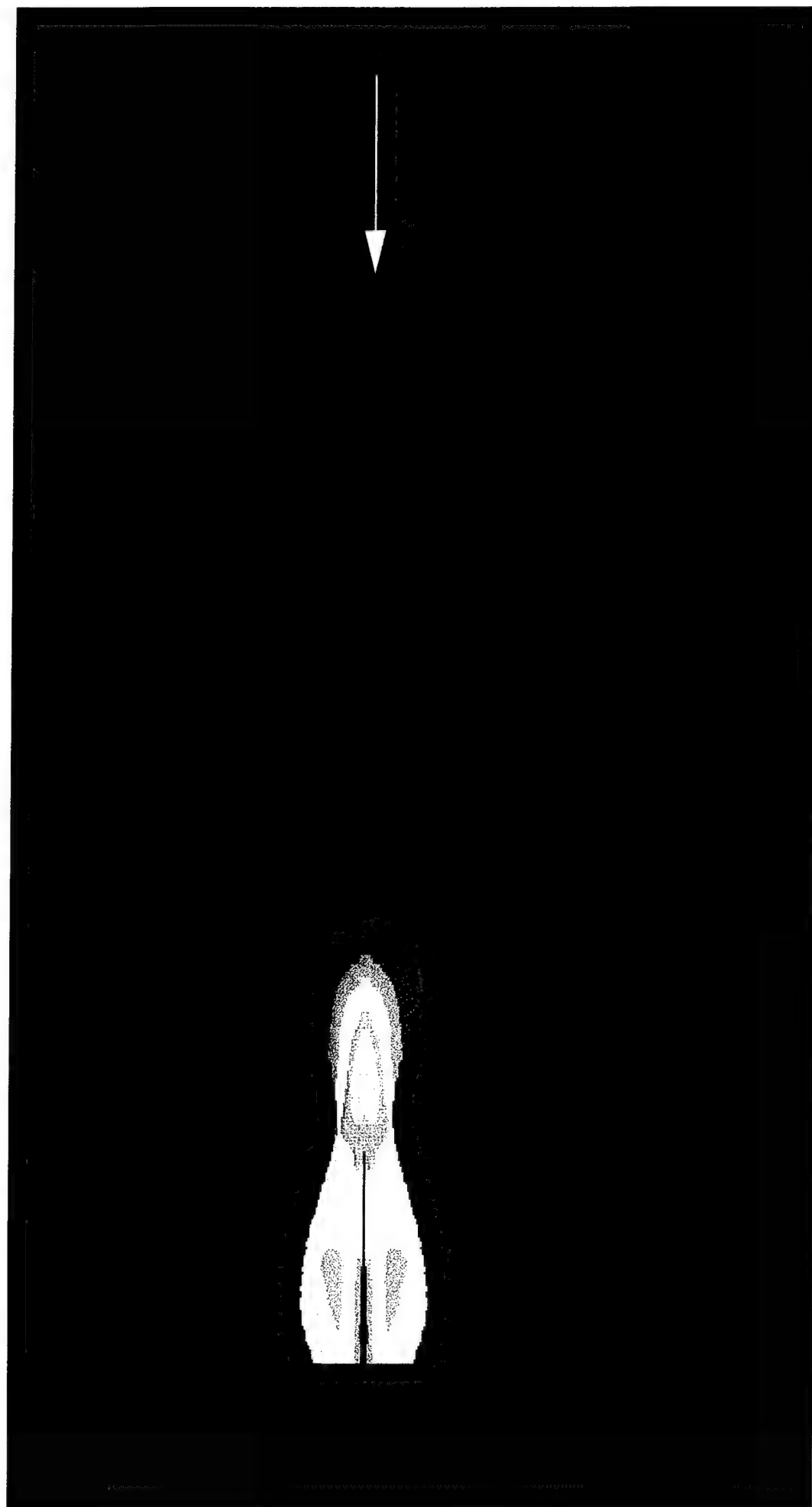


**Fig. 11**

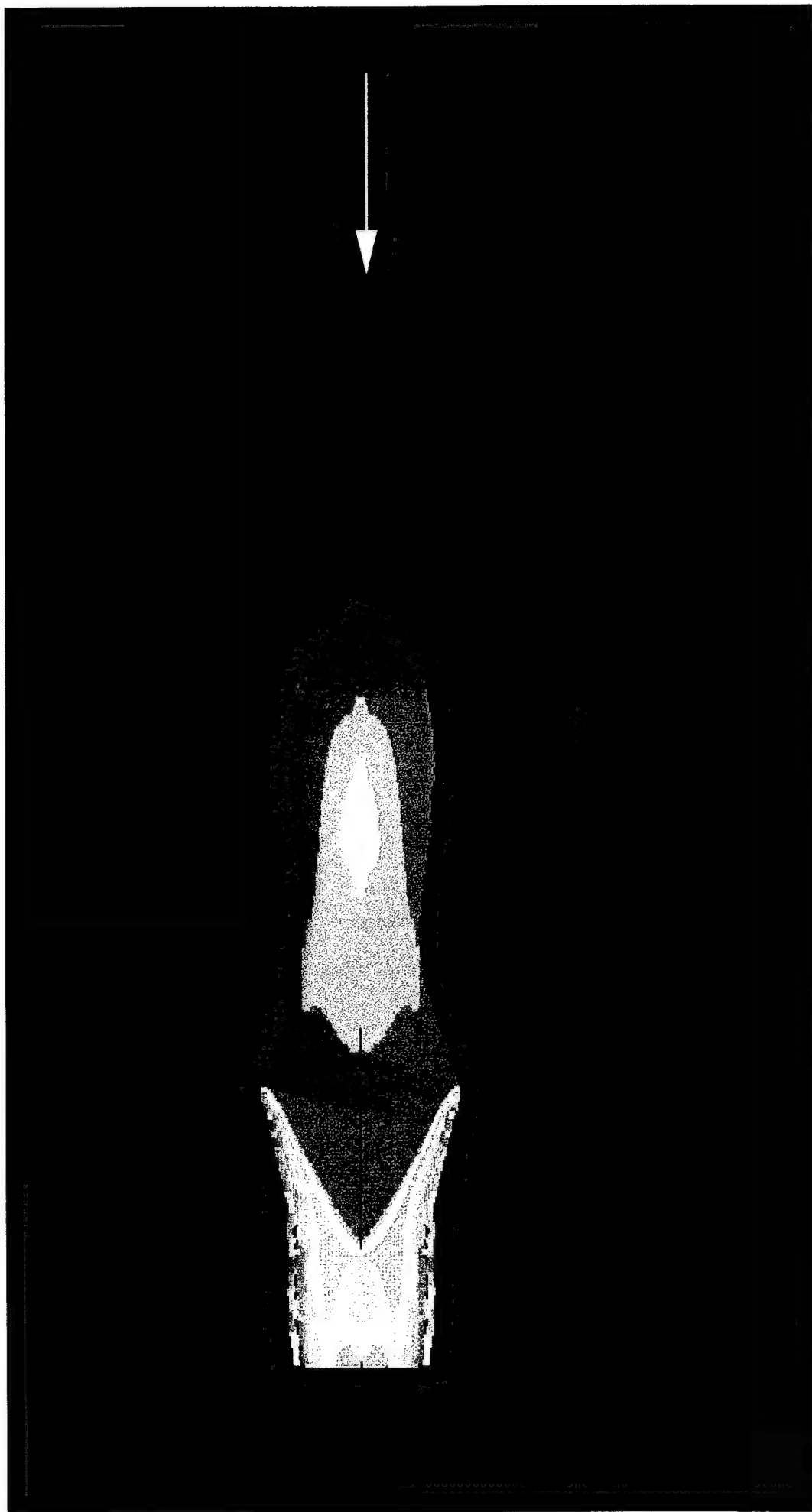


Fig. 12



Fig. 13

16	49	115	206	338	503	693	924	1188	1477
24	74	156	272	412	594	808	1048	1328	

\*1.0E+02

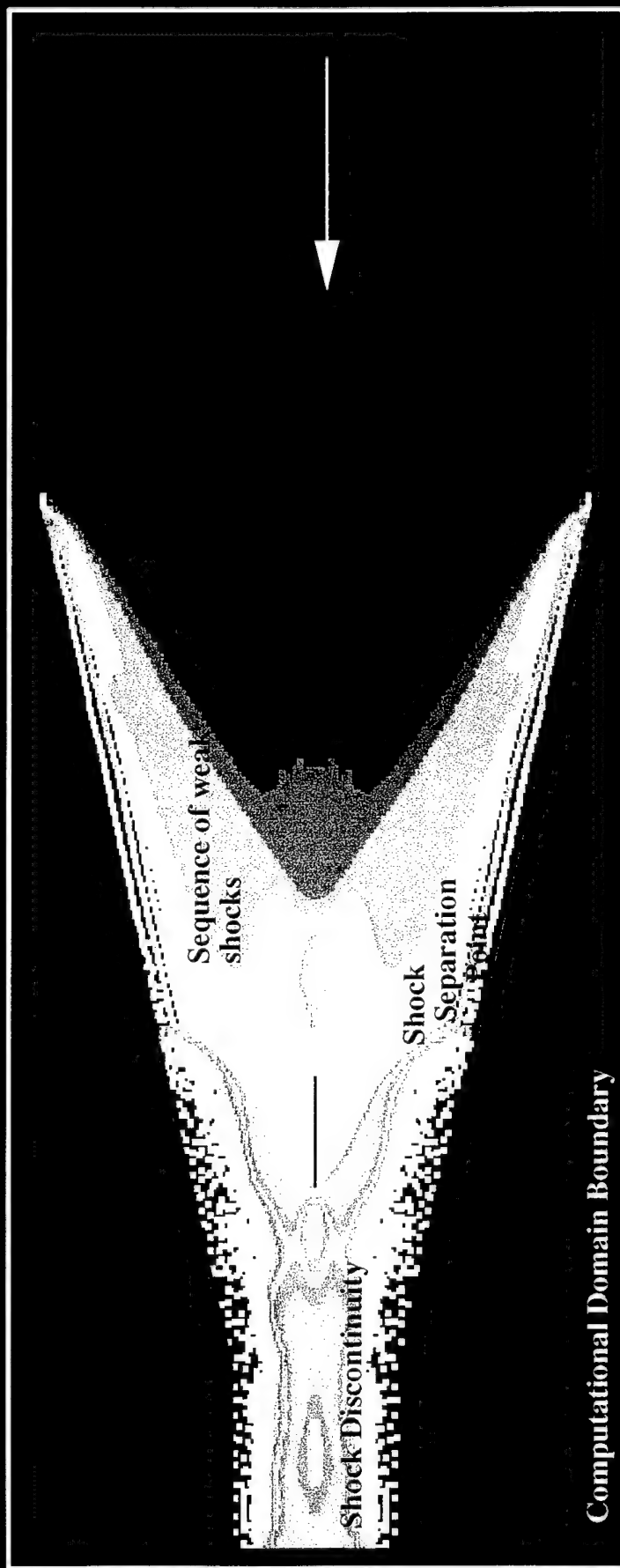
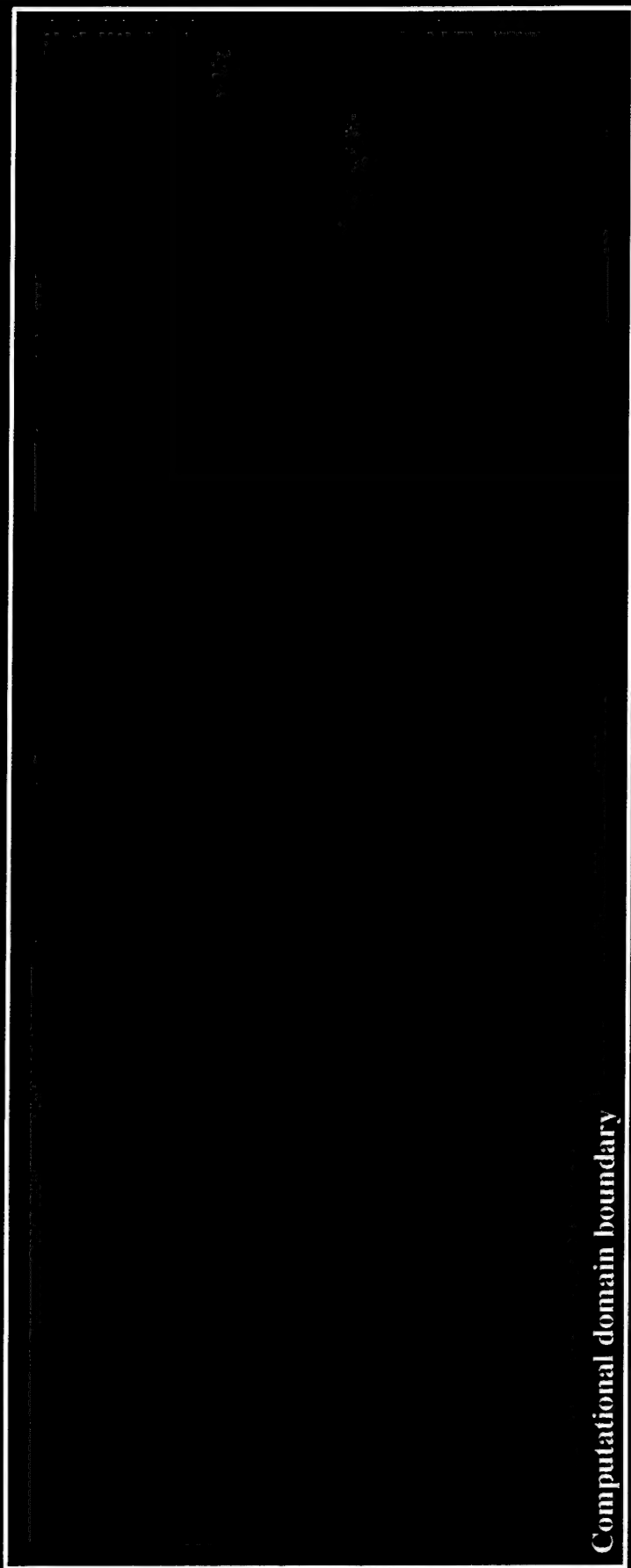


Fig. 14

16	49	115	206	338	503	693	924	1188	1477
24	74	156	272	412	594	808	1048	1328	

\*1.0E+02



Computational domain boundary

Time = 0

Fig. 15

16	49	115	206	338	503	693	924	1188	1477
24	74	156	272	412	594	808	1048	1328	

#1.0E+02

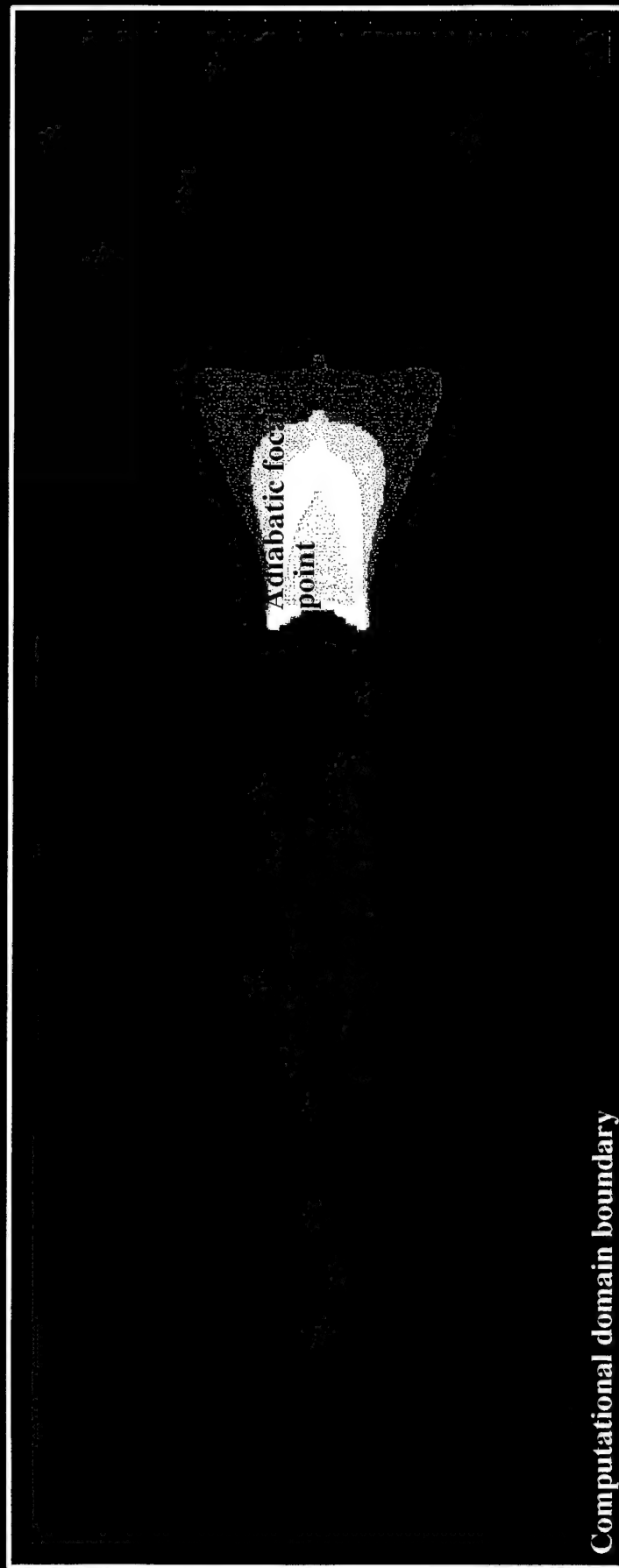


Fig. 16



16	49	115	206	338	503	693	924	1188	1477
24	74	156	272	412	594	808	1048	1328	

\*1.0E+02

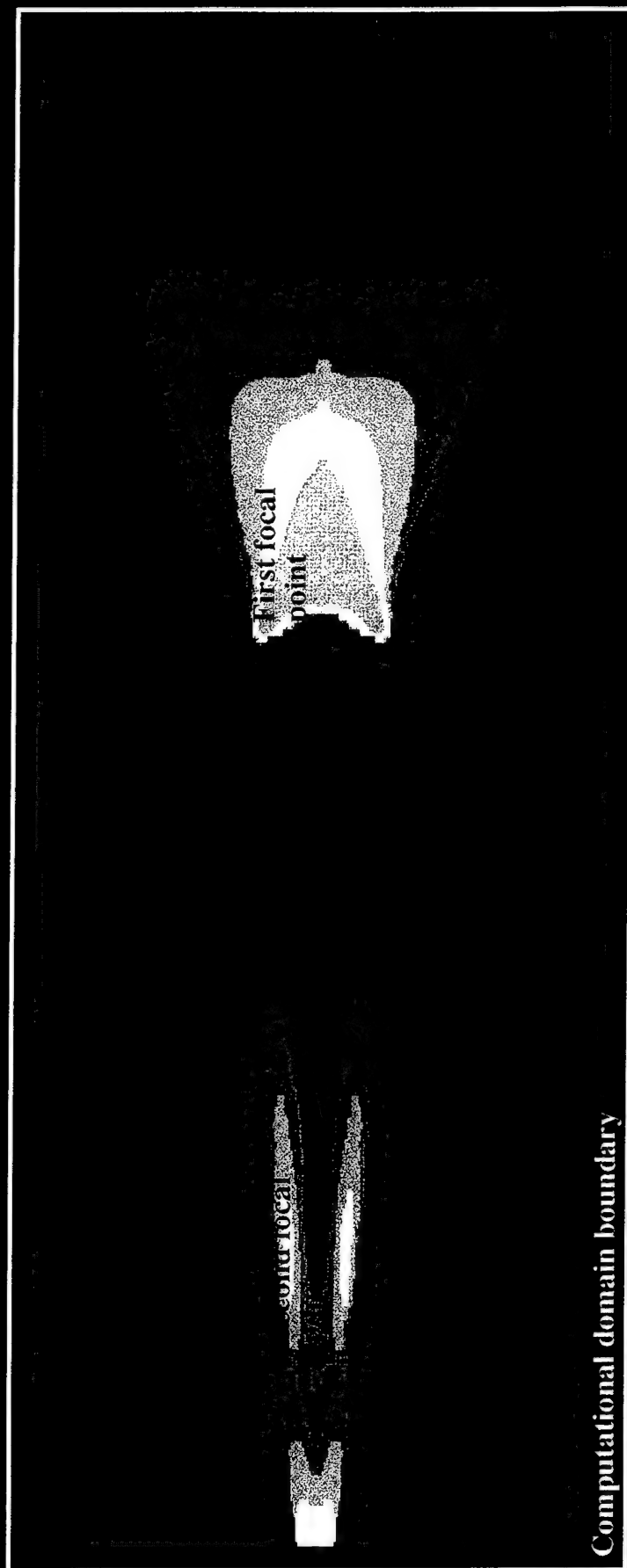


Fig. 17

16	49	115	206	338	503	693	924	1188	1477
24	74	156	272	412	594	808	1048	1328	

\*1.0E+02

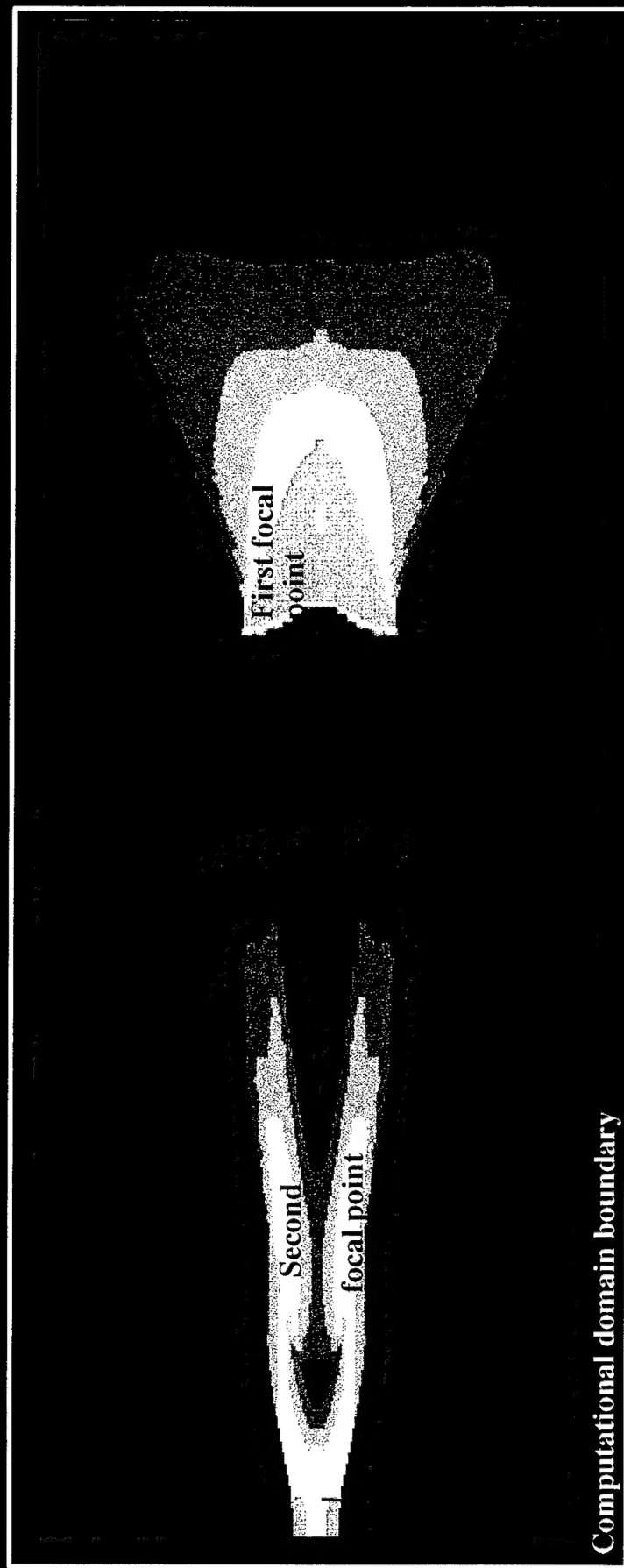


Fig. 18



Fig. 19

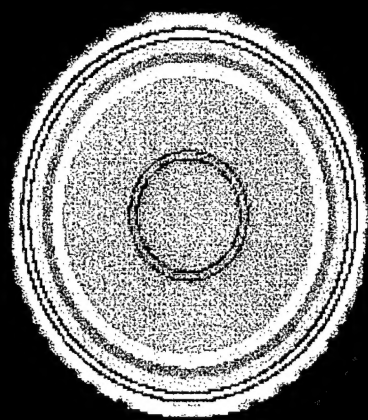
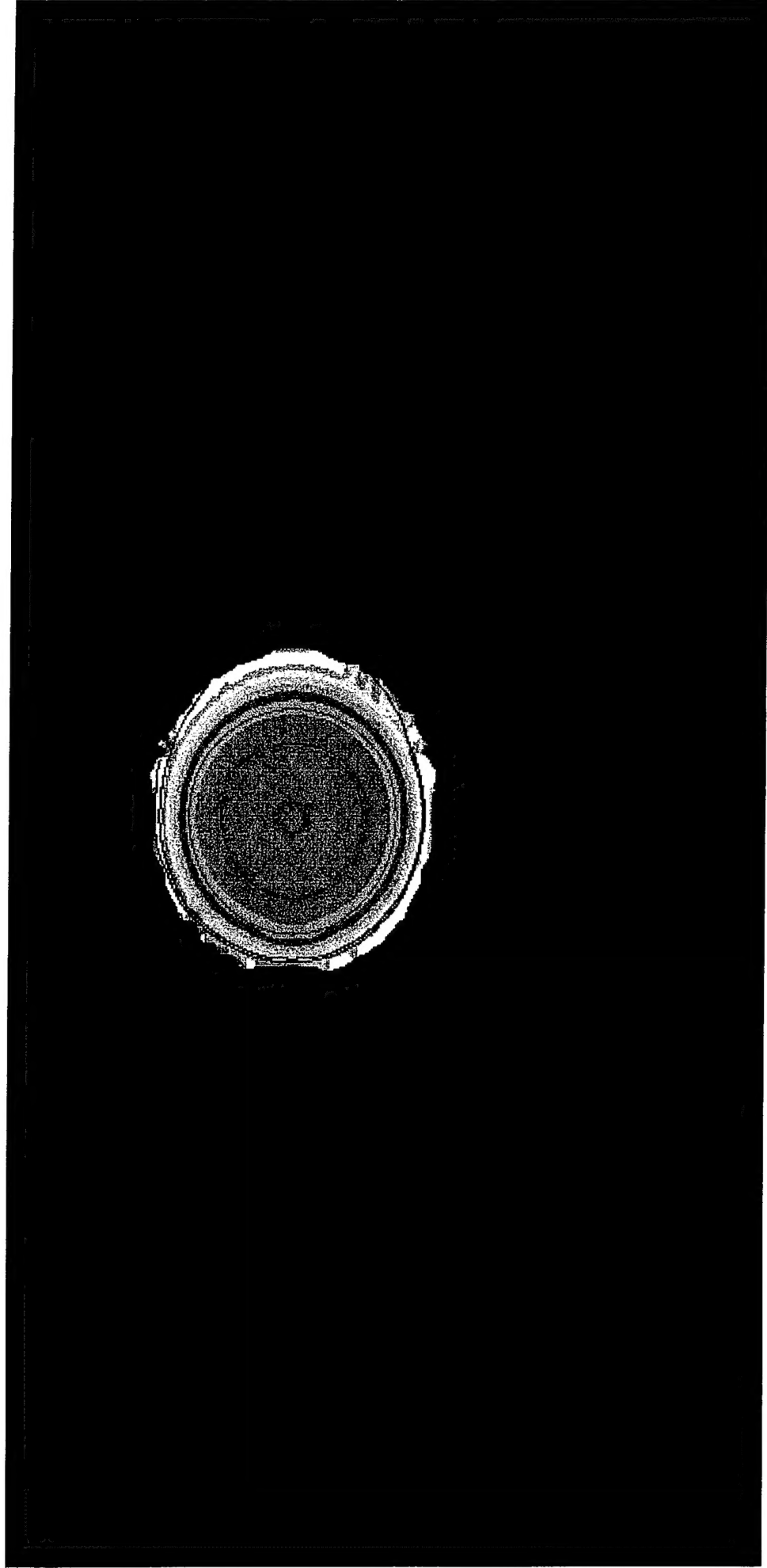


Fig. 20



**Fig. 21**